DISCRETE AND CONTINUOUS
DYNAMICAL SYSTEMS–SERIES B
Volume **2**, Number **1**, February **2002**

Website: http://AIMsciences.org

pp. **129–147**

# IDENTIFICATION OF MODULATED ROTATING WAVES IN PATTERN–FORMING SYSTEMS WITH O(2) SYMMETRY

A. Palacios

Department of Mathematics
San Diego State University
San Diego, CA 92182, USA

Abstract. A numerical algorithm for identifying Modulated Rotating Waves in spatially extended systems with **O(2)** symmetry—the symmetry group of rotations and reflections on the plane, is presented. The algorithm can be applied to numerical simulations of Partial Differential Equations (PDEs) and experimental data obtained in a laboratory. The basic methodology is illustrated with various cellular patterns obtained from video images of a combustion experiment carried out on a circular burner. Rotating waves and modulated rotating waves are successfully identified in the experiment. The algorithm is then validated by comparing the analysis of experimental patterns with the analysis of computational patterns obtained from numerical simulations of a reaction-diffusion PDE model.

1. **Introduction.** Observations from numerical and physical experiments with spatial and temporal characteristics frequently reveal a variety of nonstationary patterns that change in space and time, that is, *spatio-temporal* patterns [24, 25]. Under the presence of continuous symmetries in the experiments, it is common to observe patterns in the form of *Rotating Waves* (RWs) and Modulated Rotating Waves (MRWs). Rotating Waves are periodic solutions that appear stationary when observed in an appropriate rotating frame [20]. At all times, the shape of the wave remains constant, though the wave is rotated in space by a given angle. In contrast, Modulated Rotating Waves periodically change shape as their angular speed varies nonuniformly and periodically.

In systems with continuous symmetry, MRWs typically arise via symmetry-breaking Hopf bifurcations. Near a Hopf bifurcation, the modulations in space and time of a MRW might be indistinguishable and we may be erroneously lead to believe that the observed wave is a RW. Identifying a particular pattern as a representative of a RW or a MRW may be specially difficult when the only information available is the pattern itself. Experimentalists are usually confronted with this task. There are, however, algorithms for finding RWs and MRWs in nonlinear evolution PDEs. For instance, Barkley [1] developed a numerical method for calculating rotating spiral waves in a two–species model of an excitable medium. Brown and Kevrekidis [2] employ a Galerkin projection method for computing modulated traveling waves in the Kuramoto-Sivashinsky equation, which models flame instability. These techniques and many others depend on closed form solutions of the

1991 *Mathematics Subject Classification.* 37M20.
*Key words and phrases.* Spatio-temporal patterns, bifurcation theory, symmetry.

model. They can not be readily extended to solve the problem of identification in physical experiments because the equations of motions are rarely known.

In this work, we develop a technique for solving the identification problem of RWs and MRWs in systems with $\mathbf{O(2)}$ symmetry—the symmetry group of rotations and reflections on the plane. We demonstrate its use through the analysis of cellular flame patterns from a laboratory experiment [9, 10, 11]. The algorithm is validated by comparison with the analysis of similar patterns from numerical simulations of a PDE model [17]. In both numerical and laboratory experiments, the algorithm not only effectively identifies RWs and MRWs but it also provides a quantitative description of how the patterns are modulated in space and time. The ideas and methodology behind the technique are based on the study of bifurcations from relative equilibria by Krupa [15], and the study of Hopf bifurcations from rotating waves by Golubitsky *et al.* [7].

Following the work of Golubitsky *et al.*, we assume the observations from a numerical or laboratory experiment are described by a scalar real–valued function $u(\mathbf{x}, t) : \Omega \to \mathbb{R}$, where $\mathbf{x} \in \Omega \subset \mathbb{R}^n$ is the domain of the experiment and $t$ is time. In numerical experiments, for instance, $u$ can be a component of a vector-valued solution $U(\mathbf{x}, t)$ to a nonlinear evolution system of partial differential equations

$$\frac{dU}{dt} = F(U, \lambda),$$

where $\lambda$ is a bifurcation parameter. In a physical experiment, for instance Rayleigh-Bénard convection in which a fluid confined between two parallel plates is heated from below [25], $u$ can be assumed to be a component of a velocity field, and $\Omega = \{(x, y, z) : 0 < z < 1\}$ a region between the two plates. In both types of experiments, $u$ describes a spatially extended dynamical system. Patterns are then generated by level set curves of the observable $u$ through

$$P_u(t) = \{\mathbf{x} \in \Omega : u(\mathbf{x}, t) \geq c\},$$

where $c$ is a constant [7]. If $U(\mathbf{x}, t)$ describes a RW that rotates rigidly and uniformly with angular speed $\omega_r$, we can write $U$ in the form

$$U(\mathbf{x}, t) = R_{\omega_r t} U_0(\mathbf{x}), \tag{1}$$

where $R_{\omega_r t}$ is a rigid rotation by an angle $w_r t$, and $U_0(\mathbf{x}) = U(\mathbf{x}, 0)$. Equation (1) describes a wave pattern whose shape remains constant at all times, though at time $t$ the wave is rotated in space by an angle $\omega_r t$. If $\Gamma$ is the underlying group of symmetries of the experiment, then it follows from (1) that RWs are found only in systems where $\Gamma$ is at least $\mathbf{SO(2)}$—the continuous group of rotations on a plane.

Upon changes of parameters, rotating waves generically undergo symmetry-breaking Hopf bifurcations to Modulated Rotating Waves (MRWs) [6, 8, 21]. Numerical simulations illustrating this type of bifurcations in cellular flame patterns are shown in Bayliss *et al.* [7] and in Palacios [17]. Similar bifurcations in experiments on a circular burner can be found in Gorman [9, 10, 11]. In this latter example, the circular geometry of the burner induces reflectional symmetry in addition to $\mathbf{SO(2)}$ symmetry. Thus, the underlying group of symmetries of the experiments is $\mathbf{O(2)}$—the group of rotations and reflections on the plane. Using a center bundle construction, Golubitsky *et al.* [7] show that in a neighborhood of a bifurcation from a RW to a MRW, a MRW can be written as

$$U(\mathbf{x}, t) = R_{\omega_r t + \delta(t)} Q(\mathbf{x}, t). \tag{2}$$

where $\omega_r$ is the frequency of the average drift of the wave, $\delta(t)$ is a $T$-periodic function that modulates the rotational motion of the wave along the group orbit, and $Q(\mathbf{x}, t)$ is also a $T$-periodic function that describes the change of shape of the wave as a function of time. Thus, the temporal evolution of a MRW is characterized by two essential frequencies: $\omega_r$, frequency of average drift, and $\omega_m = 2\pi/T$ being the frequency of modulations about the rotational motion of the wave. In the absence of modulations, $\delta(t) = 0$, $Q(\mathbf{x}, t) = U_0(\mathbf{x})$, and we recover expression (1), which describes a RW.

The aim of this work is to develop a computational algorithm for identifying MRWs by decomposing observables from numerical or experimental systems through (2). More details, including illustrative examples, can be found in the following section. This paper is organized as follows. In Section 2 we explain basic mathematical ideas. The methodology behind the algorithm is then developed in Section 3. In Section 4, we illustrate the applicability of the algorithm through the analysis of cellular flame patterns produced in a combustion experiment. The algorithm is validated by comparison with the analysis of computational flame patterns obtained through numerical simulations of a reaction-diffusion PDE model.

2. **Basic Ideas.** Let $U_0$ be a rotating wave solution from a numerical or laboratory experiment with $\Gamma$ symmetry. In the study of bifurcations from relative equilibria in systems with $\Gamma$ symmetry, Krupa [15] shows that in a neighborhood of $U_0$ the vector field $F$ admits the decomposition

$$F(U) = F_{T_{U_0}}(U) + F_{N_{U_0}}(U),$$

where $F_{T_{U_0}}$ and $F_{N_{U_0}}$ are tangent and normal vector fields to group orbits $\Gamma U_0$. Both of these vector fields are $\Gamma$-equivariant. Krupa also showed that in the neighborhood of the rotating wave $U_0$ all solutions can be written as solutions of $F_{N_{U_0}}$ modulated by drifts along the group orbit, that is

$$U(\mathbf{x}, t) = \gamma(t)Q(\mathbf{x}, t),$$

where $\gamma(t)$ is a smooth curve of group elements of $\Gamma$, and $Q$ is a solution of $F_{N_{U_0}}$. Golubitsky *et al.* [7] show that observables of $U$ admit a similar decomposition

$$u(\mathbf{x}, t) = \gamma(t)q(\mathbf{x}, t), \tag{3}$$

where $u$ and $q$ are observables of solutions $U$ and $Q$, respectively.

*Rotating Waves.* Assuming that $\Gamma$ acts on $u$ by

$$\gamma u(\mathbf{x}, t) = (\gamma^{-1}\mathbf{x}, t),$$

where $\gamma \in \Gamma$, the authors further show that the observable $q$ of a rotating wave is $q(\mathbf{x}, t) = u_0(\mathbf{x})$ for all values of $t$, where $u_0(\mathbf{x}) = u(\mathbf{x}, t_0)$. That is, $q$ is constant in time. Since the wave rotates uniformly with speed $\omega_r$, then $\gamma(t) = \omega_r t$ and (3) takes the form

$$u(\mathbf{x}, t) = R_{\omega_r t}u_0(\mathbf{x}), \tag{4}$$

where $R_{\omega_r t}$ is a rotation by an angle $\omega_r t$.

The evolution of a pattern of a RW is then visualized by the level set curves

$$P_u(t) = R_{\omega_r t}P_u(0). \tag{5}$$

These curves indicate that a pattern $P_u(0)$ rotates uniformly and rigidly along the group orbit. A computational example, with state variable $\mathbf{x} \in \mathbb{R}^2$, is depicted in Figure 1. The example simulates a single–cell flame rotating clockwise over a

circular burner (see Section 4.1). As prescribed by (1), the shape of the cell remains constant at all times, though rotated by an angle in space.

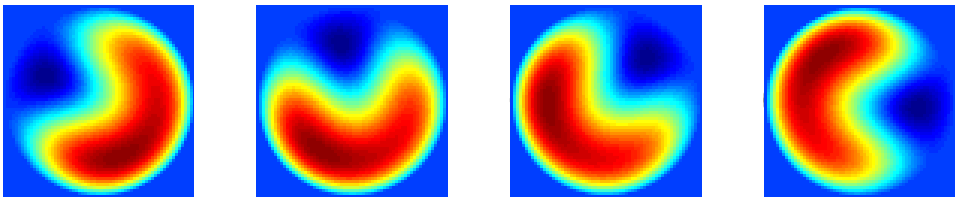


FIGURE 1. Evolution of a computational rotating wave simulating a single–cell flame in the combustion of premixed gases. The cell rotates uniformly and without changing shape.

*Modulated Rotating Waves.* Similarly, from definition (2), it can be shown that the motion along the group orbit of a MRW is of the form $\gamma(t) = \omega_r t + \delta(t)$, where $\delta$ is a periodic function in time with frequency $\omega_m$—the frequency of modulations of the average drift of the wave. Then (3) takes the form

$$u(\mathbf{x}, t) = R_{\omega_r t + \delta(t)} q(\mathbf{x}, t), \tag{6}$$

where $q$ is a periodic function in time whose period is the same as that of $\delta$. The evolution of a pattern of a MRW is then visualized through the level set curves

$$P_u(t) = R_{\omega_r t + \delta(t)} P_q(t). \tag{7}$$

In this case the level set curves describe a pattern, $P_q$, that rotates with two frequencies while its shape changes periodically. An example from a laboratory experiment, also with state variable $\mathbf{x} \in \mathbb{R}^2$, is shown in Figure 2. The example is the experimental version of the single-cell flame of Figure 1.

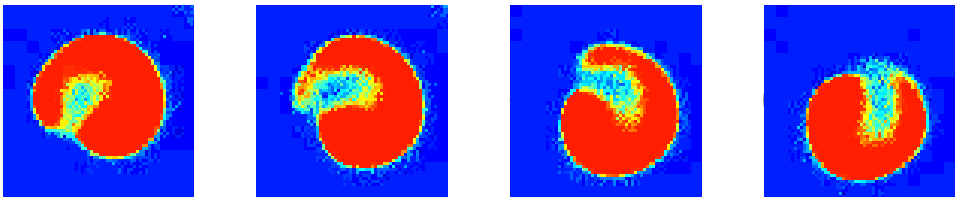


FIGURE 2. Evolution of a single-cell flame from a combustion experiment. The algorithm of Section 3 identifies this pattern as a MRW with average drift $\omega_r = 22.6726\ rad/sec$ and frequency of modulations $\omega_m = 23.1938\ rad/sec$.

Identifying the exact nature of the motion directly from visual observations may be misleading, specially when a pattern rotates as rapidly as in Figure 2. To the human eye, this single flame pattern appears to be rotating uniformly and rigidly. However, application of the algorithm presented in this work reveals two frequencies: an average drift $\omega_r = 22.6726\ rad/sec$ and a frequency of modulations

$\omega_m = 23.1938\ rad/sec$. The pattern is then classified as a MRW. The motion along the group orbit is shown in Figure 3. The negative slope is consistent with clockwise rotations. The presence of fast frequencies confirms the difficulties of a direct visual identification.

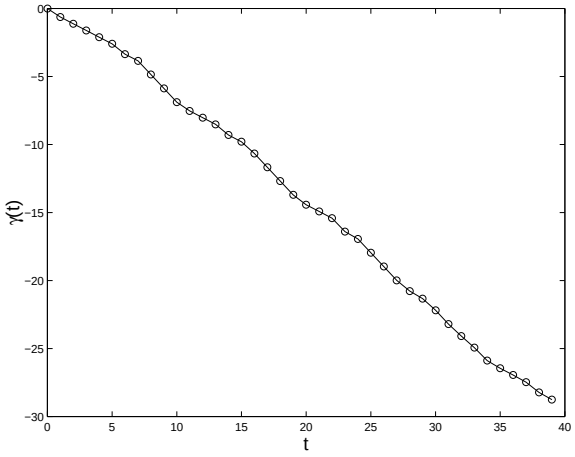


FIGURE 3. Modulated rotations $\gamma(t) = \omega_r t + \delta(t)$ in the experimental state of Figure 2.

Shape changes in the cellular flame are captured by $q(\mathbf{x}, t)$ as is shown in Figure 4. Observe that such changes are mostly visible near the "tail" of the cell. Note also that $q$ never rotates, it only oscillates in amplitude.

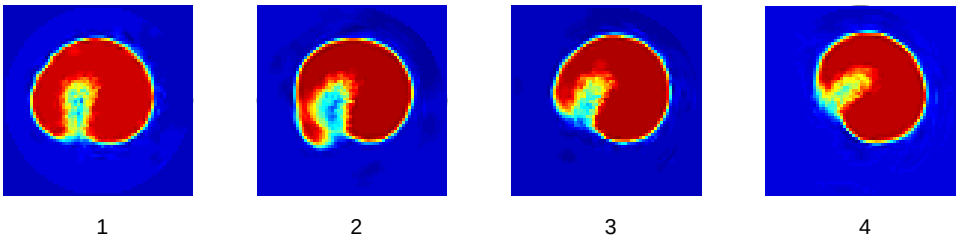


FIGURE 4. Shape changes captured by $q(\mathbf{x}, t)$ during the four snapshots of Figure 2.

A visual measure of how far a MRW is from bifurcation from a RW is provided by the inner and outer patterns of the observable $q$. Golubitsky *et al.* [7] define these patterns as

$$P^{inner} = \bigcap_t P_q(t) = \{\mathbf{x} \in \Omega \ : \ \min_t q(\mathbf{x}, t) \geq c\}$$
$$P^{outer} = \bigcup_t P_q(t) = \{\mathbf{x} \in \Omega \ : \ \max_t q(\mathbf{x}, t) \geq c\}.$$

Since a RW rotates without changing shape, it follows that its inner and outer patterns must be identical and equal to the level set curves of the observable. At a point of Hopf bifurcation, where the RW bifurcates into a MRW, the inner

and outer patterns start separating from each other. The separation is gradual and proportional to the amplitude of the MRW. For instance, Figure 5 illustrates the inner and outer patterns associated with the single-cell experimental state of Figure 2. They were computed from the shape variations of Figure 4. These patterns and the amplitudes of the modulations in $\delta$ (see Figure 3), suggest that the single–cell state is relatively close to its bifurcation from a RW.

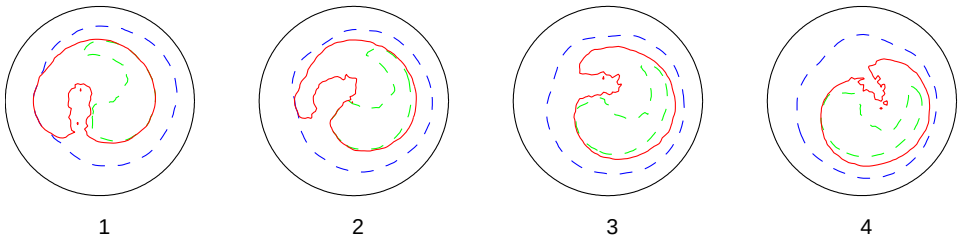


FIGURE 5. Inner (green) and outer (blue) patterns for the experimental one–cell state (red) of Figure 2.

In the next section, we show how the decomposition (8) is performed. Mainly, we show how to calculate average drifts, frequency of modulations, and shape changes, directly from the observable of a numerical or laboratory experiment.

3. **Algorithm.** We now present an algorithm for identifying MRWs directly from the observable of an experiment with $\mathbf{O(2)}$ symmetry. Let $u_0(\mathbf{x}) = u(\mathbf{x}, t_0)$ be an initial observation at time $t_0$, where $\mathbf{x} \in \mathbb{R}^n$, and let $\Gamma u_0(\mathbf{x})$ be a continuous group orbit through $u_0(\mathbf{x})$. This group orbit is $\mathbf{SO(2)}u_0(\mathbf{x})$ when $\Gamma = \mathbf{O(2)}$. Denote by $T_{u_0(\mathbf{x})}$ and $N_{u_0(\mathbf{x})}$ tangent and normal vectors to the group orbit at $u_0(\mathbf{x})$. We then seek a decomposition of the observable $u$ in the form

$$u(\mathbf{x}, t) = R_{\omega_r t + \delta(t)}\ q(\mathbf{x}, t), \tag{8}$$

where $\omega_r$ is the average drift of the wave, $\delta$ is the modulations about the average drift, and $q$ is the projection of $u$ onto the normal vector $N_{u_0(\mathbf{x})}$, see Figure 6.

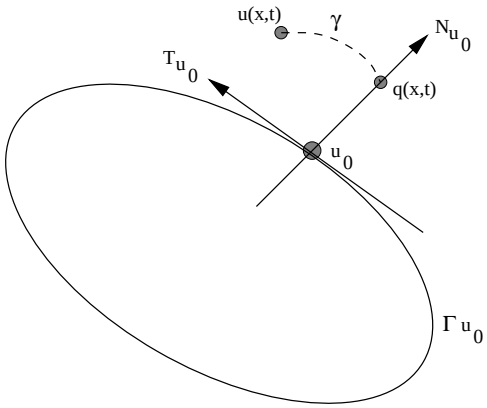


FIGURE 6. Vector field decomposition in a neighborhood of a rotating wave $u_0(\mathbf{x})$.

In physical space, $q$ models the shape changes that occur periodically in MRWs. If the period of these changes is $T$, then both $\delta$ and $q$ are also $T$-periodic functions. In the event that $u$ is a RW instead of a MRW, then we would expect to find $q = u_0(\mathbf{x})$ and $\delta = 0$ for all values of $t$. We now explain how the decomposition (8) can be achieved.

*Step 1*: Find Period of Modulations.
Compute

$$\alpha(t) = \int_\Omega u(\mathbf{x}, t)dt, \tag{9}$$

where $\Omega$ is the domain of the experiment. If $\alpha$ is constant, then the pattern described by $u$ is a wave that rotates uniformly and without changing shape. That is, $q(\mathbf{x}, t) = u_0(\mathbf{x})$ for all $t$. In this case we can write

$$u(\mathbf{x}, t) = R_{\omega_r t} u_0(\mathbf{x}).$$

where $\omega_r = 2\pi/t^*$, and $t^* > 0$ such that $\|u(\mathbf{x}, t^*) - u_0(\mathbf{x})\|$ is a minimum.

If $u$ is a MRW, however, we can expect $\alpha$ to be a $T$–periodic function in time, where $T$ is the period of the modulations along the group orbit. From the *power spectrum* [19] of $\alpha$, we first find the frequency of the modulations $\omega_m$. The period $T$ of these modulations is then given by

$$T = \frac{2\pi}{\omega_m}.$$

If the power spectrum contains more than one fundamental frequency then $u$ is not a MRW and its complexity should be analyzed with another technique [17].

*Step 2*: Compute Average Drift $\omega_r$.
We use (8) to write the initial condition $u_0(\mathbf{x})$ in the form

$$u_0(\mathbf{x}) = R_{\delta(0)} q(\mathbf{x}, 0).$$

Now let $u_T = u(\mathbf{x}, T)$. Since $\delta$ and $q$ are $T$–periodic functions, we have $u(\mathbf{x}, T) = R_{\omega_r T + \delta(0)} q(\mathbf{x}, 0)$. Alternatively, we can write

$$u_T = R_{\omega_r T} u_0(\mathbf{x}).$$

This last expression suggests how to find $\omega_r$. Define

$$\sigma^* = \min_\sigma \ \|u(\mathbf{x}, T) - R_\sigma u_0(\mathbf{x})\|$$

then

$$\omega_r = \frac{\sigma^*}{T}. \tag{10}$$

*Step 3*: Compute Temporal Modulations $\delta$ and Shape Variations $q$.
We must first find the tangent direction to the group orbit at $u_0(\mathbf{x})$ by computing

$$Ju_0(\mathbf{x}) = \left. \frac{d}{dt} R_t u(\mathbf{x}) \right|_{t=0}.$$

In experiments where the state variable is two-dimensional, $\mathbf{x} \in \mathbb{R}^2$ and this last calculation is facilitated by the use of polar coordinates $\mathbf{x} = (r, \theta)$. In such case,

we can apply the Chain rule and the fact that $R_t u(r,\theta) = u(r,\theta - t)$, to obtain the expression

$$Ju_0(r,\theta) = -\frac{\partial u_0(r,\theta)}{\partial \theta}.$$

Regardless of the dimension of the state variable, we take care of the case where $u_0(\mathbf{x}) \in Ju_0(\mathbf{x})$ by redefining the tangent direction to be

$$v_0 = Ju_0(\mathbf{x}) - (Ju_0(\mathbf{x}), u_0(\mathbf{x}))u_0(\mathbf{x}),$$

where $(Ju_0(\mathbf{x}), u_0(\mathbf{x}))$ denotes any inner product operation. In practice, it is common that observations from laboratory or numerical experiments might be available only at discrete spatial grid points, so that $\Omega = (x_1, x_2, \ldots, x_N)$, where $x_j$ is the $j$-th grid point and $u(\mathbf{x}, t_i)$ is the vector $\mathbf{u}_i = [u(x_1,t_i), u(x_2,t_i), \ldots, u(x_N,t_i)]^T$. In such cases, we can use the standard vector inner product $(\mathbf{u}_i, \mathbf{u}_j) = u(x_1,t_i)u(x_1,t_j) + \ldots + u(x_N,t_i)u(x_N,t_j)$. This type of inner product is employed in Section 4. Tangent and normal vectors (see Figure 6) to the group orbit are then defined as follows

$$\begin{aligned} T_{u_0(\mathbf{x})} &= v_0(\mathbf{x}) - u_0(\mathbf{x}) \\ N_{u_0(\mathbf{x})} &= (v_0(\mathbf{x}))^{\perp} - u_0(\mathbf{x}). \end{aligned}$$

We can now find $q$ by projecting $u$ onto $N_{u_0(\mathbf{x})}$, but observe from Figure 6 that this projection is not orthogonal. Instead, group elements $\gamma \in SO(2)$ must be applied to $u$ until $\gamma u \in N_{u_0(\mathbf{x})}$. We perform the projection in two steps. First we subtract the average drift $\omega_r$ from (8) by computing

$$s(\mathbf{x},t) = R_{-\omega_r t} u(\mathbf{x},t).$$

This last relation indicates that $s$ is equivalent to observing $u$ in a rotating frame rotating with speed $\omega_r$. Thus, if $u$ is a MRW then $s$ must be a periodic solution. The second step in the projection is to find $\theta^* \in \mathbf{SO(2)}$ so that $R_{\theta^*} s \in N_{u_0(\mathbf{x})}$. Such $\theta^*$ is found when the vectors $R_{\theta^*} s(\mathbf{x},t) - u_0(\mathbf{x})$ and $T_{u_0(\mathbf{x})}$ are orthogonal, that is, through

$$\theta^*(t) = \min_{\theta(t)} \left( R_{\theta(t)} s(\mathbf{x},t) - u_0(\mathbf{x}), T_{u_0(\mathbf{x})} \right)$$

Applying the group elements $R_{\theta^*(t)}$ to $s$ yields the shape changes of the wave

$$q(\mathbf{x},t) = R_{\theta^*(t)} s(\mathbf{x},t). \tag{11}$$

From (8), we can also see that $s(\mathbf{x},t) = R_{\delta(t)} q(\mathbf{x},t)$. It follows that the modulations in the rotational motion of the wave along the group orbit are

$$\delta(t) = -\theta^*(t). \tag{12}$$

*Step 4*: Numerical Error.
Numerical error can be introduced while carrying out the above steps. Sources of this error include: insufficient data, not enough spatial grid points, and round-off errors. In any case, the error in the approximation is quantified by

$$\epsilon(t) = \left\| u(\mathbf{x},t) - R_{\omega_r t + \delta(t)} q(\mathbf{x},t) \right\|.$$

4. **Application to Flame Dynamics.** Laboratory experiments on a circular porous plug burner confirm that premixed gases burn irregularly, causing a flame front to destabilize and form patterns [5, 9, 11]. At low pressures, the typical pattern that appears is a stable uniform flow, also called *uniform state*, with the shape of a circular luminous disk. To the experimentalist, this luminous disk looks the same if the burner is rotated by an arbitrary angle, or if the experiment is observed through a vertical mirror. It is then reasonable to identify $\mathbf{O}(\mathbf{2})$, the group of rotations and reflections on the plane, as the group of symmetries of the experiments.

Upon changes of control parameters, the instabilities dominate the system thus breaking the $\mathbf{O}(\mathbf{2})$ symmetry of the flame front and giving rise to a cellular structure. A spontaneous $\mathbf{O}(\mathbf{2})$ symmetry–breaking bifurcation from the uniform state takes place. The cellular structure that appears can become organized in stationary and nonstationary patterns in the form of concentric rings. Stationary patterns are steady states with petal–like structures and posses spatial symmetries. Nonstationary patterns are dynamical states that change continuously in space and time, and may posses spatio–temporal symmetries. The cells move either individually or collectively within the ring structure. The global dynamics could be as deterministic as a uniformly rotating wave and as complicated as an aggregation of cells moving chaotically [10]. Figure 7 illustrates a few representative cases.

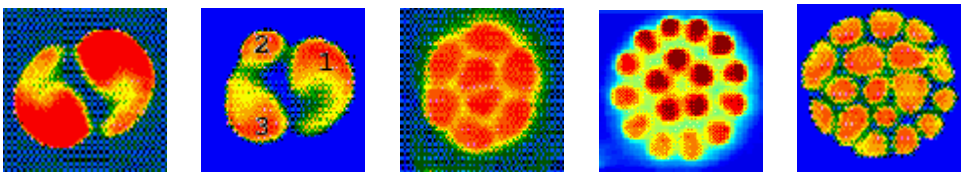


FIGURE 7. Five representative cases of nonstationary cellular flame patterns.

From left-to-right, the first pattern describes a two-cell state rotating counterclockwise; the second pattern, called *hopping state* [12], is characterized by abrupt and sequential changes in angular positions of individual cells while the cells rotate around the ring; in the third pattern, two concentric rings rotate in opposite directions; the fourth pattern, called *ratcheting*, describes an nonstationary outer ring that rotates abruptly while the inner ring remains stationary; the last pattern represents a disordered state [13].

In these experiments, RWs are nonstationary patterns that appear to be stationary when observed in an appropriate rotating frame. The cells rotate rigidly and their shape remains constant. In the transition to the chaotic regime, RWs typically undergo a Hopf bifurcation leading to MRWs. The cells now change shape periodically as they rotate, and the patterns that they produce appear to be periodic solutions when observed in an appropriate rotating frame.

Before we apply the algorithm of Section 3 to some of the experimental states described above, we first develop insight into the properties of the bifurcations and instabilities in the experiments through the aid of a phenomenological model. The model is capable of producing cellular patterns with characteristics that resemble those of the experiment. These computational patterns can be used for validating the algorithm presented in this work.

4.1. **Computational Patterns.** We simulate the formation and evolution of cellular flame patterns in circular domains through the integration of a reaction–diffusion PDE model of the form

$$\begin{aligned} \partial_t u &= (B-1)u + A^2 v - \eta u^3 - \nu_1(\nabla u)^2 + \kappa_1 \nabla^2 u \\ \partial_t v &= -Bu - A^2 v - \eta v^3 - \nu_2(\nabla v)^2 + \kappa_2 \nabla^2 v, \end{aligned} \tag{13}$$

where $u(\mathbf{x},t)$ and $v(\mathbf{x},t)$ are two linearly coupled, diffusive spatio-temporal fields with diffusion coefficients $\kappa_1$ and $\kappa_2$, respectively, and $\mathbf{x} \in \mathbb{R}^2$. The cubic terms control the growth of the linearly unstable modes, while the nonlinear gradient terms render the model nonvariational. In previous work [17], several stationary and nonstationary patterns with similar characteristics to the experimental states were observed in the model. In this work, we use patterns computed from solutions of (13) for the purpose of obtaining insight into the type of bifurcations that lead to experimental states with rotating cells. In order to simulate the circular geometry of the burner, we integrate (13) in polar coordinates $\mathbf{x} = (r,\theta)$ over a circular grid of radius $R$. An Alternating Direction Implicit Algorithm is used in the numerical integration procedure [19]. Since qualitatively different patterns are observed as $R$ is varied, the radius of the burner will be treated as a distinguished bifurcation parameter.

4.1.1. *Linear Stability Analysis.* A scalar field $u(r,\theta,t)$ satisfying Dirichlet boundary conditions on a circular domain of radius $R$ can be expanded as

$$u(r,\theta,t) = \sum_{n,m} z_{nm}(t)\Psi_{nm}(r,\theta) + c.c.$$

where $\Psi_{nm}(r,\theta) = J_n(\alpha_{nm} r/R)e^{in\theta}$, ($m \geq 0$ and $n > 0$) and *c.c.* denotes complex conjugate [26]. Here $J_n(r)$ is the $n^{th}$ order Bessel function of the first kind and $\alpha_{nm}$ is its $m^{th}$ nontrivial zero. $z_{nm}$ are complex time-dependent coefficients, save for $z_{0m}$ which are real. The orthonormality and completeness of the functions $\{\Psi_{nm}(r,\theta)$: $n \geq 0$, $m \geq 1$ $\}$ gives

$$z_{nm}(t) = \frac{1}{\pi R^2 J_{n+1}^2(\alpha_{nm})} \int_0^{2\pi} \int_0^R r\, u(r,\theta,t)\bar{\Psi}_{nm}(r,\theta)\; d\theta dr,$$

with the proviso that the coefficients are half of the value given when $n = 0$.

Previously, the linear stability of the uniform state $(u_0(\mathbf{x}), v_0(\mathbf{x})) = (0,0)$ was studied by considering small perturbations $w = (w_u, w_v)$ proportional to Fourier–Bessel functions

$$w = e^{\lambda t}\; \Psi_{nm}(r,\theta).$$

Under these perturbations, the uniform state $(u_0(\mathbf{x}), v_0(\mathbf{x}))$ is stable if $\lambda < 0$, and unstable if $\lambda > 0$. The marginal stability curve corresponds to those parameters where $\lambda = 0$ and is calculated as a function of the distinguished parameter $R$

$$B_{nm}^M(R) = 1 + \frac{\kappa_1}{\kappa_2}A^2 + \kappa_1\Big(\frac{\alpha_{nm}}{R}\Big)^2 + \frac{A^2}{\kappa_2}\Big(\frac{R}{\alpha_{nm}}\Big)^2. \tag{14}$$

Beyond this curve, on increasing $B$, the uniform state destabilizes to $\Psi_{nm}(r,\theta)$. For a given value of $A$, a particular curve $B_{nm}$ reaches a minimum value of

$$B_0 = 1 + \frac{\kappa_1}{\kappa_2}A^2 + 2A\sqrt{\frac{\kappa_1}{\kappa_2}}$$

at a radius $R = \alpha_{nm}\left(\frac{\kappa_1\kappa_2}{A^2}\right)^{1/4}$. The results presented in this paper are evaluated with fixed values of $\kappa_1 = 0.2$, $\kappa_2 = 2.0$, $\eta = 2.0$, $\nu_1 = 0.5$, $\nu_2 = 1.0$, and $A = 5.0$. $B$ and $R$ are used as control parameters.

4.1.2. *Numerical Examples.* Integration of the phenomenological model (13) is carried out in a hybrid computing cluster of DS10 Compaq workstations, and in a 8-node Alpha (21164)-based Beowulf cluster. Without loss of generality, we choose to focus the integration in a region where the evolution of a single cell can be traced. Such region can be found in a neighborhood of the marginal stability curves $B_{11}$ and $B_{21}$ as is shown in Figure 8. In this neighborhood, Fourier–Bessel modes $\Psi_{11}$ and $\Psi_{21}$ compete for stability. In physical space, these modes are patterns with one and two cells, respectively.

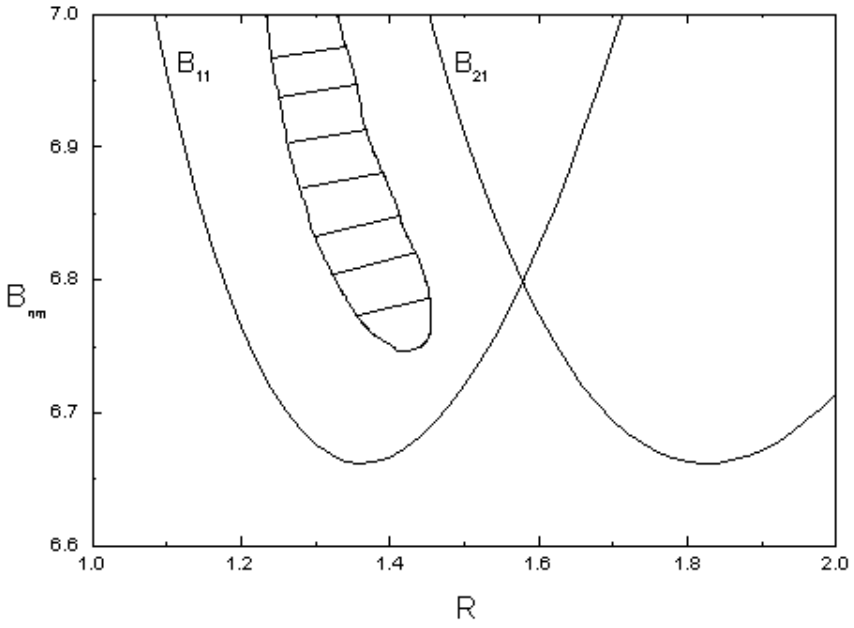


FIGURE 8. Marginal stability curves.

To the left of the shaded region in Figure 8, a stationary pattern with one cell is observed. Crossing the shaded region (on moving right) a symmetry–breaking Hopf bifurcation is encountered. The cell then loses stability, its reflectional symmetry is broken, and the cell starts to rotate clockwise, see Figure 1. From (9), we find $\alpha$ to be constant and then classify the single-cell state as a RW. Continuing moving right, the RW undergoes another Hopf bifurcation and as result, the shape of the cell starts changing periodically, see Figure 9.

The algorithm of Section 3 was coded in C and implemented in a Sun Ultra 60 workstation with two processors. Application of the coded algorithm reveals that $\alpha(t)$, see equation (9), is a T-periodic function in time. Since T is the period of

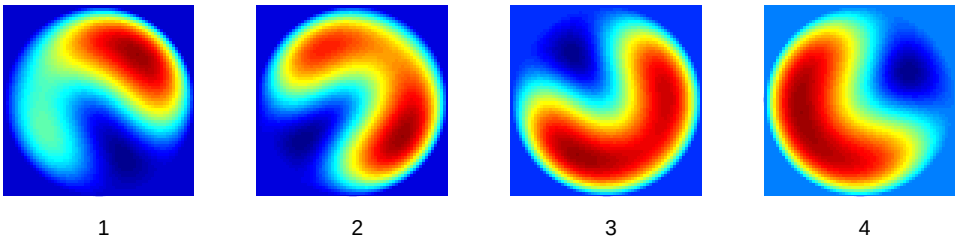


FIGURE 9. Evolution of a computational modulated rotating wave.

the modulations about the rotational motion of the cell, it then follows that the computational pattern of Figure 9 might indeed be a MRW. The power spectrum of $\alpha$ then yields $\omega_m = 0.039062\ rad/sec$. This is the frequency at which the cell changes its shape while it rotates. Further calculations through (10) yield an average drift $\omega_r = 0.06849\ rad/sec$, which is consistent with the slow rotational motion that is visually calculated in the computer animations. The motion along the group orbit is shown in Figure 10. The negative slope of $\gamma$ indicates clockwise rotations. Finally, the pattern is classified as a MRW.

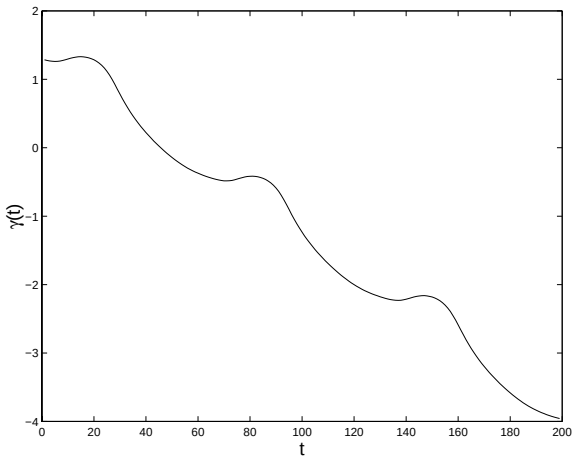


FIGURE 10. Modulated rotations $\gamma(t) = \omega_r t + \delta(t)$ in the computational state of Figure 9.

A visual indication of how far the MRW is from bifurcation is provided by the inner and outer patterns. These patterns measure minimum and maximum shape changes throughout the evolution of an observable. They are computed from $q$ based on (8). Although the inner and outer patterns are stationary, we can apply the group orbit to them and verify that $\gamma(t)P^{inner} \subset P_u(t) \subset \gamma(t)P^{outer}$. A complete animation reveals that $P_u(t)$ makes contact, at least at one time, with every point of $P^{inner}$ and $P^{outer}$. Figure 11 shows a few snapshots of an animation coinciding with those of Figure 9.

4.2. **Experimental Patterns.** We now use the insight obtained in the analysis of computational patterns to study the experimental patterns described earlier in

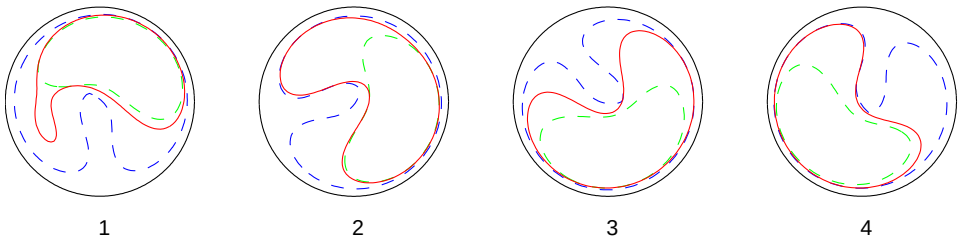


FIGURE 11. Inner (green) and outer (blue) patterns for the computational modulated rotating wave (red) of Figure 9.

this section. We concentrate the analysis to states with rotating cells. These states are typically found in isobutane-air flames. In order to capture the spatio-temporal characteristics of the flame, the evolution of the flame front is recorded with a Dage-MTI CCD camera. The video images capture the emitted chemiluminescence from the flame front and provide a two-dimensional measurement proportional to the temperature at various points on the burner. Such measurements are commonly used in flame models [3, 22, 23].

4.2.1. *Single–Ring Rotating States.* Figure 12 shows four snapshots of an experimental state in which a single-ring of two cells rotates counter-clockwise. A total of forty snapshots, extracted at the rate of 30/frames per second, were digitized for this case.

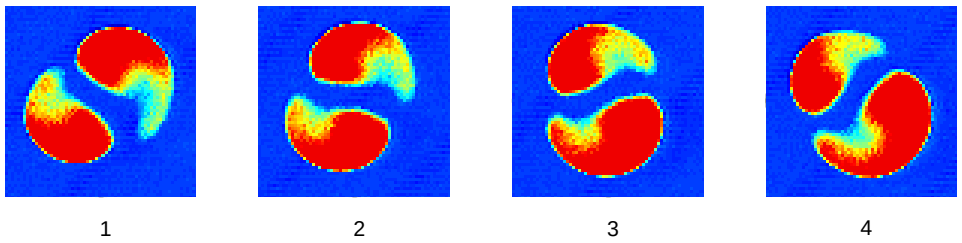


FIGURE 12. Snapshots of a single-ring experimental state describing a RW with two cells.

We find $\alpha$ to be almost constant. Thus suggesting that the motion along the group orbit is almost linear. To compute the average drift it then suffices to set $T > 0$, so that $u(\mathbf{x}, T)$ can be any of the snapshots except the one used for $u(\mathbf{x}, 0)$. As described in Step 2, we then rotate $u(\mathbf{x}, T)$ until the norm difference with respect to $u(\mathbf{x}, 0)$ is minimum. This yields the almost linear group motion with average drift $\omega_r = 16.5087$ *rad/sec* as is shown in Figure 13. The positive slope of $\gamma$ indicates counter-clockwise rotations, and the actual value of $\omega_r$ is consistent with visual measurements of the angular velocity. It is then reasonable to classify this pattern as a RW. Similar calculations were performed to classify the experimental pattern shown in Figure 2.

4.2.2. *Multiple–Ring Rotating States.* At a pressure of 1/2 *atm*, most of the observed experimental states have two concentric rings of cells. Nonstationary states

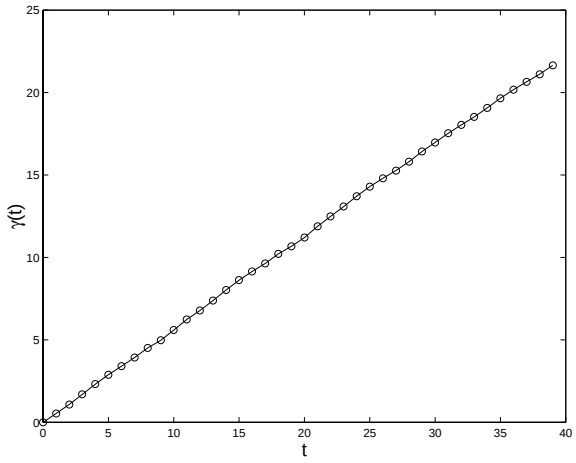


FIGURE 13. Uniform rotations $\gamma(t) = \omega_r t$ in the experimental state of Figure 12.

with rotating cells appear in various configurations. We consider first a state with two concentric rings of six and two cells, see Figure 14.

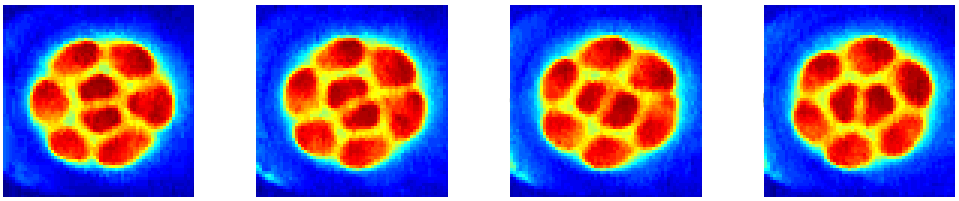


FIGURE 14. Snapshots from a counter-rotating rings state in the combustion experiment.

The outer ring rotates clockwise at a speed of about $360^0$ $/sec$, while the inner ring rotates counter-clockwise at almost twice the speed of the outer ring. In previous work [18], we determined that the dynamics of the rings uncouples. Thus the rings can be treated separately and we choose to analyze the inner ring. After completing Step 1-3 of the algorithm, we find $\delta(t)$ to be a well-defined periodic function. Using this $\delta$ function we find the frequency $\omega_m = 28.3478\ rad/sec$, which quantifies how often the cells in the inner ring change shape. Adding $\omega_r t$ to $\delta(t)$ then reveals the nature of the periodic modulations along the group orbit. These modulations can be clearly seen in Figure 15. The positive slope of $\gamma$ indicates that the inner ring rotates counter-clockwise with angular speed $\omega_r = 14.8383 rad/sec$, approximately. It is then reasonable to classify the inner ring as an example of a MRW.

Shape changes in this MRW are difficult to visualize due to the small size of the cells in the inner ring. Such changes, although small in amplitude, are captured by $q$ as is shown in Figure 16.

Substituting $q$ and $\gamma(t)$ in (8), we can then reconstruct the evolution of the inner ring, see Figure 17. The modulations in this ring are visible during a complete

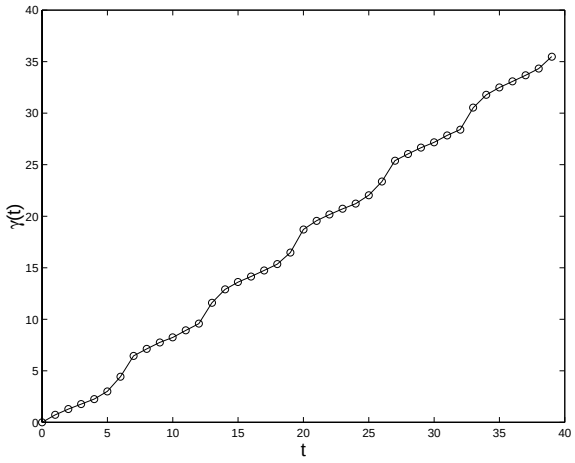


FIGURE 15. Modulated rotations $\gamma(t) = \omega_r t + \delta(t)$ for the experimental state of Figure 14.

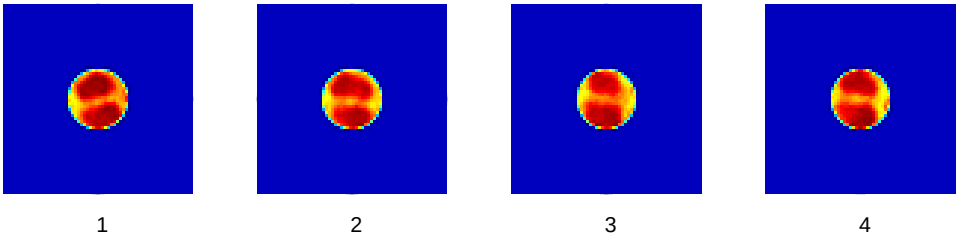


FIGURE 16. Shape changes in the inner ring of Figure 14.

animation of the reconstructed data. A similar decomposition of the outer ring was performed as well. Interestingly, the results (not shown to avoid repetitiveness) reveal that the outer ring, however, rotates uniformly and rigidly as a RW. Thus this multiple ring state is an example where a RW coexists with a MRW.

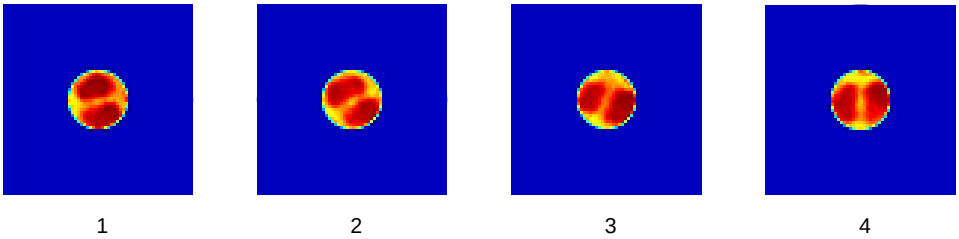


FIGURE 17. Reconstruction of the motion of the inner ring of Figure 14 using (8).

*Ratcheting State.* More complicated behavior in multiple ring states is observed in the so called *ratcheting states*[14]. The dynamics of these states is characterized by a slow (approximately $1^0$ $/sec$) drifting of symmetric rings punctuated by periods

of abrupt, faster angular displacement. In this section, we unravel the dynamics of a particular ratcheting state labeled *rat12w5*. This state describes an outer ring with 12 cells that ratchets around a stationary inner ring with 5 cells. Figure 18 shows four snapshots of the motion taken at equal length intervals.

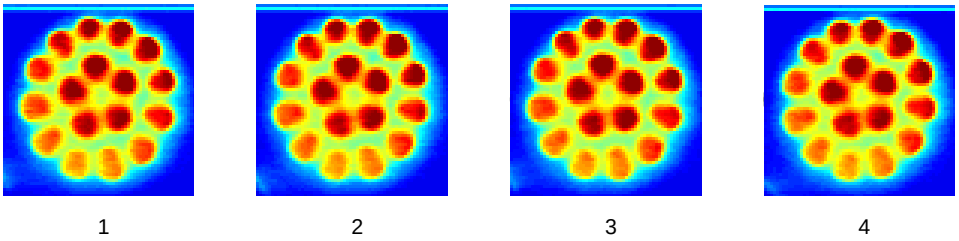


FIGURE 18. A ratcheting experimental state: the outer ring slowly drifts counter-clockwise with punctuated periods of abrupt, faster angular displacements. The inner rings remains stationary with distinctive $\mathcal{D}_5$ spatial symmetry (symmetry of a pentagon).

Since the motion of the ratcheting ring is slow, a large number of video frames was digitized, 500 exactly. The capturing rate was reduced from 30 (previous examples) to 4 $frames/sec$. The decomposition reveals, see Figure 19, time intervals of strong modulations followed by intervals where the outer ring becomes almost stationary. The existence of these intervals reflect the abrupt changes in angular speed described above. Specifically, two angular frequencies were calculated: an average drift $\omega_r = 0.0139\ rad/sec$ and a frequency of modulations $\omega_m = 1.7187\ rad/sec$. These results are consistent with the visual measurements reported in [14]. We then classify the ratcheting state rat12w5 as another example of a MRW.

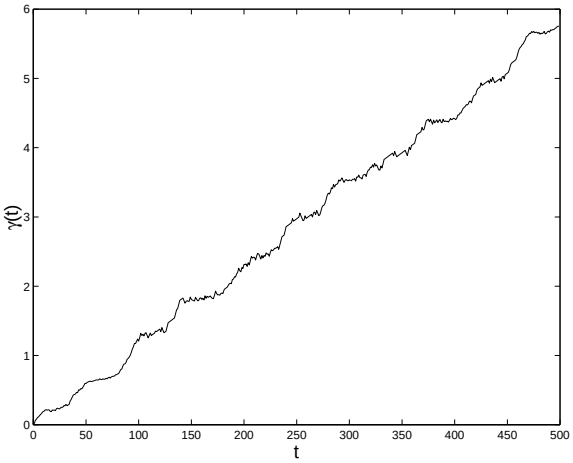


FIGURE 19. Modulations in the motion of the experimental ratcheting state of Figure 18.

The regions where the outer ring changes speed can be enhanced by increasing the digitization rate. Such adjustment is limited by the digitization equipment and by the amount of memory that is required to store the large number of video frames

that would follow. As an alternative approach, we choose to focus the attention to smaller time intervals while keeping the capturing rate constant. For instance, we consider the first 100 frames of Figure 19. A similar decomposition is performed and the motion along the group orbit is now illustrated in Figure 20. This second decomposition provides a better resolution of the complexity of ratcheting motion. Specifically, the decomposition shows that the modulations of the ratcheting ring form a well-defined staircase shape. In this staircase, we can see that the outer ring slows down, approximately, on intervals of equal length: $[50 : 150]$ and $[250 : 350]$. The accelerations that follow the slow motion of the ring also occur during intervals of similar length: $[150 : 250]$.

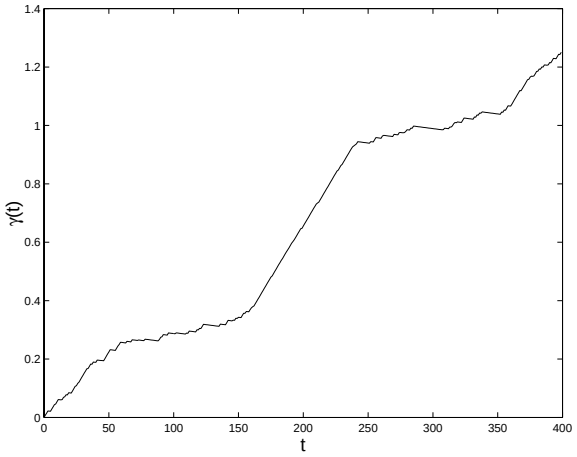


FIGURE 20. Enhancement of modulations in the ratcheting state of Figure 18.

Shape changes are again difficult to visualize due to the small size of the cells. Only the nonuniform distribution in the intensity of the flame across the cells is visible in $q$, see Figure 21. This nonuniformity may be due to experimental noise in the burner or in the digitization equipment.

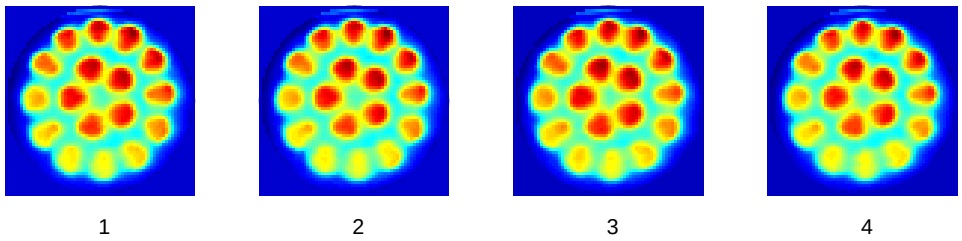


FIGURE 21. Shape changes in the ratcheting state of Figure 14.

We now use the motion along the group orbit described by Figure 19 to reconstruct the original pattern. The result is shown in Figure 22. An animation of the reconstructed dynamics gives the visual perception of ratcheting in the outer ring. The outer ring is observed to slow down and accelerate periodically as is seen in the experiments.

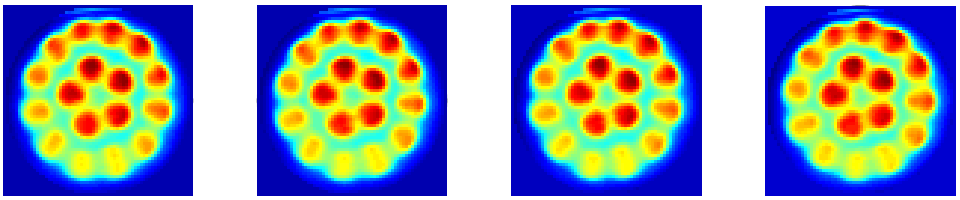


FIGURE 22. Reconstruction of the motion of the ratcheting state of Figure 18 using (8).

5. **Discussion.** I have identified RWs and MRWs in four experimental flame states: (1) a single cell state (MRW), (2) a two-cell state (RW), (3) two counter-rotating rings (RW and MRW), and (4) ratcheting state (MRW). One distinctive and common feature in all these patterns is the lack of reflectional symmetry in the cells. This spatial feature can be explained as follows. If a cellular state has certain symmetries at one instant of time, then it must have the same symmetries at all times. Consequently, any cellular state with reflectional symmetry must have the same symmetry at all times and it therefore cannot rotate. Hopping states were also studied and their analysis revealed, in contrast to MRWs, the absence of an average drift. In related work [16], we then showed that hopping states arise from the interaction of two RWs as opposed to the Hopf bifurcation from a RW that leads to MRWs. It is my hope that this work can be extended to study other pattern-forming systems with various symmetry properties.

**Acknowledgments.** I would like to thank M. Golubitsky, M. Gorman, G. Gunaratne, and I. Melbourne for many useful discussions and suggestions.

## REFERENCES

[1] D. Barkley, LINEAR STABILITY ANALYSIS OF ROTATING SPIRAL WAVES IN EXCITABLE MEDIA, Phys. Rev. L, 68, no. 13, (1992), 2090-2093.
[2] H. Brown and I. Kevrekidis, MODULATED TRAVELING WAVES FOR THE KURAMOTO-SIVASHINSKY EQUATION, Pattern Formation: Symmetry Methods and Applications (J. Chadam and W. Langford, eds.), Fields Institute Communications, 5, AMS, (1995), 45-62.
[3] A. Bayliss and B. Matkowsky, NONLINEAR DYNAMICS OF CELLULAR FLAMES, SIAM J. Appl. Math. 52, no. 2, (1992), 396-415.
[4] A. Bayliss, B. Matkowsky, and H. Riecke, SYMMETRIES IN MODULATED TRAVELING WAVES IN COMBUSTION: JUMPING PONIES ON A MERRY-GO-ROUND, Pattern Formation: Symmetry Methods and Applications (J. Chadam and W. Langford, eds.), Fields Institute Communications, 5, AMS (1995), 19-43.
[5] J. Buckmaster ed., "The mathematics of Combustion", SIAM, Philadelphia, (1985).
[6] J.D. Crawford, M. Golubitsky, and W. Langford, MODULATED ROTATING WAVES IN $\mathbf{O}(\mathbf{2})$ MODE INTERACTIONS, Dynam. and Stabil. of Syst., 3, (1988), 159-175.
[7] M. Golubitsky, V. LeBlanc, and I. Melbourne, HOPF BIFURCATION FROM ROTATING WAVES AND PATTERNS IN PHYSICAL SPACE, J. Nonlinear Sci., 10 (2000), 69-101.
[8] M. Golubitsky, I. Stewart, and D.G. Schaeffer, "Singularities and Groups in Bifurcation Theory", Vol. 2, Springer-Verlag, New York, (1988).
[9] M. Gorman, M. el-Hamdi, and K. Robbins, A PICTUREBOOK OF DYNAMICAL MODES OF FLAT, LAMINAR PREMIXED FLAMES, Technical Report #2, University of Houston, (1990).
[10] M. Gorman, C. Hamill, M. el-Hamdi, and K. Robbins, ROTATING AND MODULATED ROTATING STATES OF CELLULAR FLAMES, Combust. Sci.and Tech., 98 (1994), 25-35.

[11] M. Gorman, M. el-Hamdi, K. Robbins, Experimental observation of ordered states of cellular flames, Combust.Sci.and Tech., 98 (1994), 37-45.
[12] M. Gorman, M. el-Hamdi, K. Robbins, Hopping motion in ordered states of cellular flames, Combust. Sci. and Tech., 98 (1994), 71-78.
[13] M. Gorman, C. Hamill, M. el-Hamdi, and K. Robbins, Four types of chaotic dynamics in cellular flames, Combust. Sci. and Tech., 98 (1994), 79-93.
[14] M. Gorman, M. el-Hamdi, B. Pearson, and K. Robbins, Ratcheting motion of concentric rings in cellular flames, Phys. Rev. L, 76, no. 2 (1994), 228-231.
[15] M. Krupa, Bifurcations of relative equilibria SIAM J. Math. Anal., 21 (1990), 1453-1486.
[16] A. Palacios, M. Gorman, and G. Gunaratne, *Modal decomposition of hopping states in cellular flames*, Chaos, 9 (1999), 755-767.
[17] A. Palacios, G. Gunaratne, M. Gorman, and K. Robbins, *Cellular pattern formation in circular domains*, Chaos **7** (1997), 463-475.
[18] A. Palacios, G. Gunaratne, M. Gorman, Karhunen-Loéve analysis of spatiotemporal flame patterns, Phys. Rev. E, 57, no. 5, (1997) 5958-5971.
[19] W. Press, S. Teukolsky, W. Vetterling, and B. Flannery, "Numerical Recipes in C", Cambridge University Press, New York, (1994).
[20] D. Rand, Dynamics and symmetry. Predictions for modulated waves in rotating fluids, Arch. Rat. Mech. Anal., 79, (1982) 1-38.
[21] M. Renardy, *Bifurcation from rotating waves*, Arch. Rat. Mech. Anal., 79, (1982) 49-84.
[22] L. Sinay, F. Williams, An analytical approach to the description of nonadiabatic cellular flames near extinction, SIAM J. Appl. Math., 52, no. 2 (1992), 416-427.
[23] G. Sivashinsky, Nonlinear analysis of hydrodynamic instability in laminar flames. Part I. Derivation of basic equations, Acta Astraunica, 4 (1977), 1177-1206.
[24] A. Turing, The chemical basis of morphogenesis, Phil. Trans. Roy. Soc. Lond., B237, (1952), 37-72.
[25] D. Walgraef, Spatio-temporal Pattern Formation Springer-Verlag, New York, (1997).
[26] G. Watson, "A treatise on the Theory of Bessel Functions", Cambridge University Press, Cambridge, (1962).

Received April 2001; revised October 2001.

*E-mail address*: palacios@euler.sdsu.edu